Check for updates

ASME Journal of Electrochemical Energy Conversion and Storage
Online journal at:
https://asmedigitalcollection.asme.org/electrochemical

Swapnil S. Salvi
Southwest Research Institute,
6220 Culebra Road,
San Antonio, TX 78238
e-mail: swapnil.salvi@swri.org

Bapiraju Surampudi
Southwest Research Institute,
6220 Culebra Road,
San Antonio, TX 78238
e-mail: bapiraju.surampudi@swri.org

Andre Swarts
Southwest Research Institute,
6220 Culebra Road,
San Antonio, TX 78238
e-mail: andre.swarts@swri.org

Jayant Sarlashkar
Southwest Research Institute,
6220 Culebra Road,
San Antonio, TX 78238
e-mail: jayant.sarlashkar@swri.org

Ian Smith
Southwest Research Institute,
6220 Culebra Road,
San Antonio, TX 78238
e-mail: ian.smith@swri.org

Terry Alger
Southwest Research Institute,
6220 Culebra Road,
San Antonio, TX 78238
e-mail: terry.alger@swri.org

Ankur Jain[1]
Department of Mechanical and Aerospace Engineering,
University of Texas at Arlington,
Arlington, TX 76010
e-mail: jaina@uta.edu

Experimental and Theoretical Analysis of Immersion Cooling of a Li-Ion Battery Module

Overheating of Li-ion cells and battery packs is an ongoing technological challenge for electrochemical energy conversion and storage, including in electric vehicles. Immersion cooling is a promising thermal management technique to address these challenges. This work presents experimental and theoretical analysis of the thermal and electrochemical impact of immersion cooling of a small module of Li-ion cells. Significant reduction in both surface and core temperature due to immersion cooling is observed, consistent with theoretical and simulation models developed here. However, immersion cooling is also found to result in a small but non-negligible increase in capacity fade of the cells. A number of hypotheses are formed and systematically tested through a comparison of experimental measurements with theoretical modeling and simulations. Electrochemical Impedance Spectroscopy measurements indicate that the accelerated cell aging due to immersion cooling is likely to be due to enhanced lithium plating. Therefore, careful consideration of the impact of immersion cooling on long-term performance may be necessary. The results presented in this work quantify both thermal and electrochemical impacts of a promising thermal management technique for Li-ion cells. These results may be of relevance for design and optimization of electrochemical energy conversion and storage systems.
[DOI: 10.1115/1.4063914]

Keywords: Li-ion batteries, immersion cooling, modeling and simulation, battery performance and reliability, thermal management

1 Introduction

Li-ion cells play a key role in energy storage and conversion in electric vehicles (EVs) and several other engineering systems. Improving the energy density and discharge rates in battery packs is of critical importance for maximizing the performance and driving range of EVs. A key technical challenge here is the strong temperature sensitivity of Li-ion cells, including rapid performance degradation at both low and high temperatures [1,2]. Moreover, serious safety concerns related to thermal runaway and fire occur when the battery temperature exceeds a certain threshold [3]. Therefore, a well-designed thermal management system for the automotive battery pack is critical [4]. Since experimental measurements may often be time-consuming and expensive, the development of robust theoretical models and numerical simulations is essential for scientific understanding and engineering optimization [3].

A vast amount of past work on modeling and simulations for battery thermal management is already available, for both steady-state [5] and transient [6] conditions. A conjugate analytical model for flow cooling of a battery pack has been proposed [7]. Thermal resistance network-based modeling has been carried out to predict the performance of an air-cooling system coupled with a micro heat pipe array for cooling a prismatic battery pack [8].

[1]Corresponding author.

Manuscript received July 25, 2023; final manuscript received October 15, 2023; published online November 30, 2023. Assoc. Editor: Soumik Banerjee.

Copyright © 2023 by ASME

Downloaded from http://asmedigitalcollection.asme.org/electrochemical/article-pdf/doi/10.1115/1.4063914/7063724/jeecs_21_4_041001.pdf by Southwest Research Institute user on 30 November 2023

Multiscale multidomain modeling has been carried out for a liquid-cooled Li-ion battery pack of 24 prismatic cells, which claims to maintain the peak temperature in the battery pack under 40 °C and maximum temperature difference across the whole battery pack around 5 °C even at a discharge rate of 5 C [9]. Another study using COMSOL Multiphysics has been carried out to compare forced air convection, heat pipe, and heat pipe with copper sheets, for which, an improvement in temperature uniformity of 39%, 67%, and 73%, respectively, has been reported [10]. Analytical models have also been used to predict the internal temperature of a Li-ion cell, which is an important parameter that is difficult to measure directly [11–14]. Thermal simulation models that account for the dynamics of electrochemical heat generation have also been reported [15,16]. Several studies have modeled thermal effects using resistance network techniques [15–21]. The sub-modeling technique has been used for resolving the large variation in length scales in thermal simulation of a large battery pack comprising thousands of cells [22].

Key battery thermal management techniques include cooling based on air [23,24], liquid [25,26], heat pipe [12,27], thermoelectric [28,29], and phase change materials [30,31]. Hybrid approaches that combine multiple techniques have also been reported [32–34]. Among these techniques, immersed liquid cooling offers very high efficiency due to high heat capacity and heat transfer coefficient, reduced equipment cost, and lower thermal expansion compared to phase change materials (PCMs) [30]. Unlike cooling by liquid flow in serpentine tubes between cells, immersion cooling enables direct cell-coolant contact, leading to greater heat dissipation, and thus reduced thermal runaway propagation [35,36]. Experimental investigation of immersion liquid cooling for a battery pack and comparison with a thermal management system based on serpentine tubes between rows of cells has been presented previously [35]. In another work, a 47% reduction in battery pack peak temperature at 3 C discharge rate was reported for immersion cooling with a dielectric fluid compared to natural convective cooling [36]. A study of preheating the battery pack in a cold ambient using a hot fluid flowing around the battery in an immersed arrangement has been reported. It was found that preheating resulted in very good temperature uniformity, within 4 °C throughout the battery pack [37]. A numerical study of fast-charging of a Li-ion battery pack based on direct immersion cooling using hydrofluoroether showed improved energy density and lower coolant pump power consumption [38]. Despite the clear benefits of immersion cooling, however, there remains a lack of work that investigates the impact of immersion cooling on the electrochemical performance of the battery pack. Such concerns may arise, for example, due to prolonged exposure to the dielectric fluid and the possibility of non-uniform cooling of cells during immersion cooling.

This paper presents an experimental and simulations-based investigation of the thermal and electrochemical impact of immersion cooling during fast charging of a Li-ion cell module. The module is subjected to a fast charge duty cycle comprising fast charge profiles interspersed with rest periods and nominal discharge for up to five weeks. A Reference performance test (RPT) is carried out each week to characterize aging effects by measuring discharge capacity fade, power fade, and resistance growth. Electrochemical impedance spectroscopy (EIS) measurements are carried out to identify possible degradation mechanisms in Li-ion batteries such as lithium plating and their effects. Analytical and numerical simulation models are developed to identify the dominant thermal and electrochemical effects of immersion cooling. A comparison between measurements and models is carried out in order to help understand the impact of immersion cooling on cell aging, and possible underlying mechanisms.

The rest of this paper is organized as follows: Sec. 2 describes the experimental setup and measurements carried out in this work. Section 3 presents a theoretical heat transfer model and simulations carried out to model the system-level thermal dynamics during immersion cooling and to estimate cell internal temperature. Key results are discussed in Sec. 4, followed by conclusions in Sec. 5.

2 Experimental Apparatus

Despite the significant potential for effective thermal management of Li-ion cells using immersion coolants, there are no standards available for evaluating the performance of immersion coolants. This section describes an experimental test bed for investigating the immersion cooling of a battery pack. Key experimental details, including cells, coolants, measurement setup, and process, are described as follows.

2.1 Experimental Setup. A seven-cell module shown in Fig. 1(*a*) is constructed using LG Chem (Seoul, South Korea) M50T 21700 cylindrical cells with lithium nickel manganese cobalt oxide (NMC) cathode and graphitic anode. This is a commonly used Li-ion cell chemistry. The nominal cell capacity is 18.2 Wh. The manufacturer-specified cell impedance of 30 mΩ [39] is assumed to remain constant. As shown in Fig. 1(*a*), the cells are interconnected in a 7PS1 configuration using spot welding on Nickel metal bus bars to form a flower-shaped cross section. The cell-to-cell gap is approximately 0.5 mm and remains fixed. Omega K-type thermocouples are glued using thermal paste and taped on the cylindrical surface of each cell. The SBT-2050 Power Cycler from PEC Corp., Boca Raton, FL, is used for implementing a fast charge current profile. Data acquisition from all thermocouples is carried out using an National Instruments (Austin, TX) Compact-RIO-based data acquisition system.

In addition, for experiments involving internal temperature measurements, the central cell in the flower configuration of the 7PS1 module is drilled axially from the negative tap side (Fig. 1(*b*)). The drill bit is handled carefully to avoid damage to the jelly roll inside the cell. Once the thermocouples are inserted inside the cell, the opening is quickly sealed with marine epoxy [11,40]. The locations of thermocouples for testing during baseline and

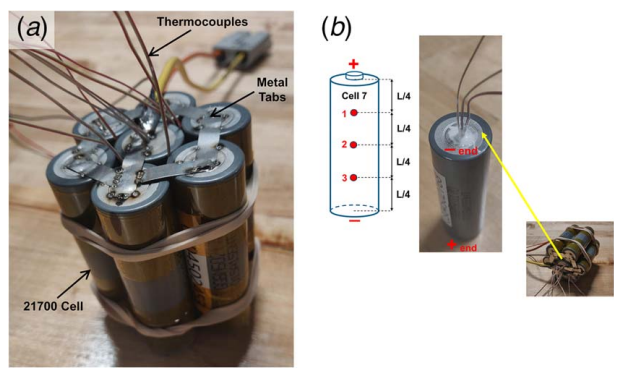

Fig. 1 Pictures of experimental setup for immersion cooling of a seven-cell battery pack: (*a*) Module of seven 21700 cells tabbed together in 7PS1 arrangement and (*b*) central cell instrumented with thermocouples in the core at locations as shown

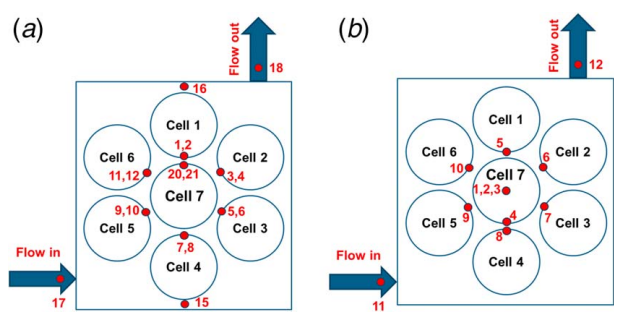

Fig. 2 Thermocouple locations for (*a*) surface and (*b*) core temperature measurement (thermocouples 1–3 as shown). The schematics are drawn as viewed from the positive terminal end of the cells.

Downloaded from http://asmedigitalcollection.asme.org/electrochemical/article-pdf/doi/10.1115/1.4063914/7063724/jeecs_21_4_041001.pdf by Southwest Research Institute user on 30 November 2023

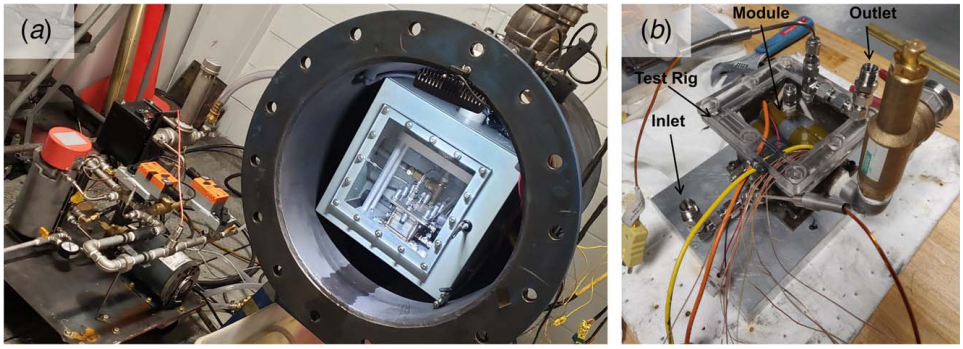

Fig. 3 (*a*) Test enclosure with coolant setup and (*b*) instrumented test rig along with the module

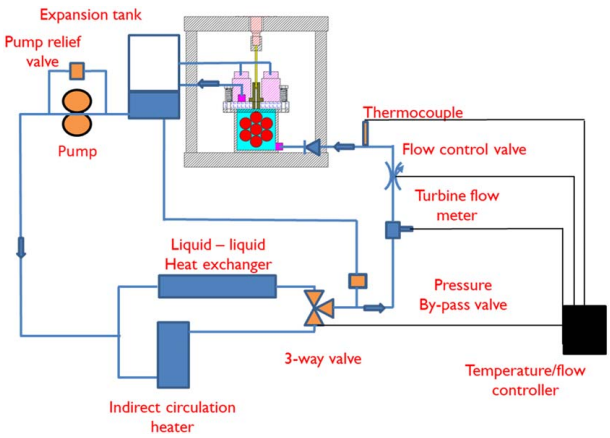

Fig. 4 Schematic of the test setup showing the fluid flow circuit and associated instrumentation

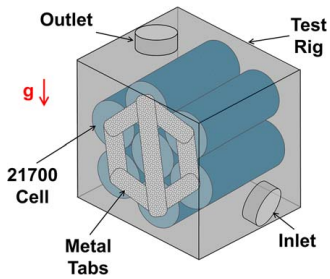

Fig. 5 Schematic showing the experimental setup for immersion cooling of seven-cell battery module

immersion cooling cases are shown in Fig. 2(*a*). For the experiment with internal temperature monitoring, thermocouples are also placed in the core cavity of the jelly roll of the cell, as indicated by locations 1, 2, and 3 in Figs. 1(*b*) and 2(*b*).

Figure 3 presents pictures of the overall experimental setup and the specific test rig that houses the battery pack. Figure 4 shows a schematic of the fluid flow circuit and related instrumentation. The module is positioned centrally in the test rig, which is customized to allow coolant flow around the cells. The test rig is large enough to accommodate the module with a clearance of around 5 mm between the outer cells and walls of the test rig. This avoids direct electrical contact and offers sufficient space for thermocouples and other essential wirings from the module to the cell cycler. At a flowrate of 1.5 liters per minute (LPM), the liquid sweeps out the entire coolant volume in the test rig every 10–20 s. The test rig is designed with only 38% excess fluid volume compared to the volume of seven cells, resulting in a compact configuration with minimum add-on weight to remain conducive for practical applications. Coolant flowrate and temperature are controlled using a flow control valve and a three-way mixer valve, respectively, as shown in Fig. 4. The mixer valve mixes cold fluid from a heat exchanger leg and hot fluid from the heater leg to produce the target temperature. As shown in Fig. 5, the fluid inlet and outlet are on one of the side faces and the top face, respectively. Both are instrumented with thermocouples to measure inlet and outlet coolant temperatures. In addition to baseline measurements without any immersion cooling, fast charge aging tests are also conducted for a single-phase immersion coolant liquid, referred to as "Fluid X." Thermal conductivity, heat capacity, and mass density of the liquid are 0.143 $Wm^{-1}\,K^{-1}$, 2.1 $kJkg^{-1}\,K^{-1}$, and 806 kgm^{-3}, respectively.

Experiments are conducted using K-type thermocouples to measure the surface temperatures of the battery cells. It is important to note that K-type thermocouples have associated uncertainties in temperature measurements, around ±1–2 °C. To minimize measurement errors, the placement of thermocouples is carried out carefully. Measurements are repeated multiple times to ensure consistency and repeatability.

2.2 Experimental Procedure. Measurements are carried out with two key goals—to evaluate cell performance and capacity fade due to multi-week cycle aging, and to monitor the internal temperature of the cell for a few cycles carried out in a 24-hour period. Performance with immersion cooling at 1.5 LPM flowrate and 25 °C inlet temperature is compared with the baseline case with no immersion cooling.

The module undergoes charge–discharge cycling for 5 days, as shown in Fig. 6(*a*), followed by RPT on the sixth and seventh days, as shown in Fig. 6(*b*). Charge–discharge cycling comprises 1 hour of rest period, followed by constant current constant voltage (CCCV) charging at a C-rate of 0.7 C, which is the maximum continuous current specification, then 1 hour rest, and finally constant current (CC) discharge at 0.2 C, corresponding to the nominal current. The module is cycled between 4.2 V and 2.5 V. Cell capacity at the end of each charge–discharge cycle is determined by charging the module at 0.3 C rate under CCCV conditions to 100% SOC and then discharging at 0.2 C rate under CC conditions to measure the static capacity in Amp-hours. Note that per battery nomenclature, the C-rate of a charge/discharge process refers to the reciprocal of the number of hours taken to complete the process. The larger the C-rate, the more aggressive is the process.

There are three components to the RPT, as shown in Fig. 6(*b*). Static capacity measurement assesses the energy storage capability of a cell by measuring its capacity to deliver a constant current over a specified time, typically at a slow discharge rate. In contrast, power capacity measurement evaluates the ability to deliver high currents for brief durations, often in seconds or less, representing its power output potential under load. Finally, pulse power fade measurement focuses on the ability to sustain repeated high-current pulses, simulating real-world, high-demand scenarios. These three

Downloaded from http://asmedigitalcollection.asme.org/electrochemical/article-pdf/doi/10.1115/1.4063914/7063724/jeecs_21_4_041001.pdf by Southwest Research Institute user on 30 November 2023

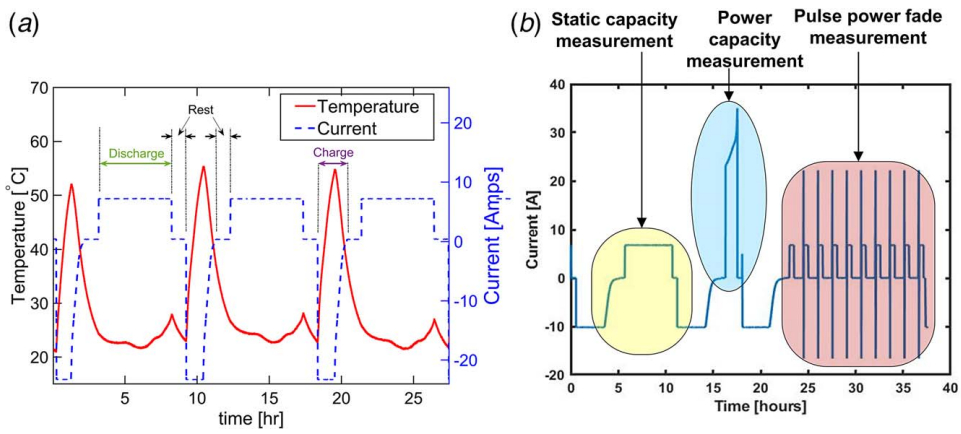

Fig. 6 (*a*) Typical current profile used for testing. The corresponding temperature curve is also shown. (*b*) A typical RPT profile.

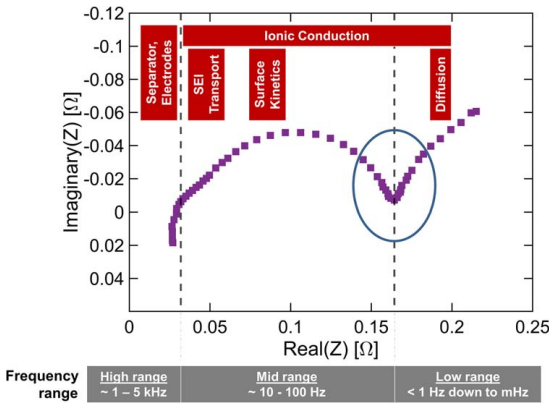

Fig. 7 A representative Nyquist plot from EIS measurements, with the minima associated with lithium plate phenomenon shown [42]

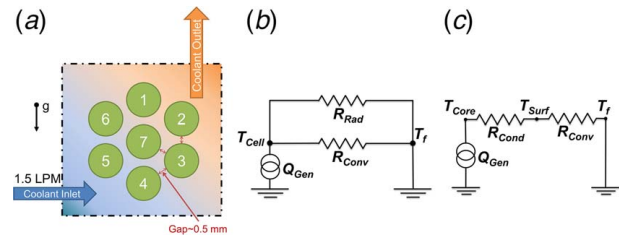

Fig. 8 (*a*) Schematic description for problem definition, (*b*) thermal resistance network (considering effective radiation) and (*c*) thermal resistance network (considering core temperature along with cell surface temperature)

measurements are interconnected—static capacity provides insights into total energy storage, power capacity quantifies the ability to meet sudden power demands, and pulse power fade testing reveals how these characteristics evolve under stress or repeated use, which is essential for optimizing battery performance and lifespan in applications like electric vehicles and portable electronics. The RPT shown schematically in Fig. 6(*b*) combines each of these measurements to obtain a comprehensive picture of the health of the module at any given time. RPT similar to the present work has been used in past work to understand how cell characteristics change during cyclic aging [41].

EIS is a non-invasive frequency response technique to highlight electrochemical phenomena within a cell, including patterns of lithium plating. Each EIS measurement is carried out while the pack is in ambient air at 25 °C. A Gamry 1010 EIS analyzer (Warminster, PA) is used to stimulate the cell with sinusoidal currents of amplitude 20 mA with frequencies from 0.1 Hz to 5 kHz. The resulting frequency response Nyquist plot in the complex domain helps understand the lithium plating process and other internal electrochemical processes [42]. For example, Fig. 7 shows a typical Nyquist plot showing different frequency regimes that may be used to understand different transport processes that occur within the cell. Specifically, the minima shown in Fig. 7 provide information about the nature of lithium plating in the cell. Since this method is ex-situ, an impulse response-based pseudo-EIS procedure [43] is also carried out. This procedure can be carried out real time or in situ during life testing or in an actual battery management system (BMS) in a vehicle or grid storage. The real impedance value is extracted from both types of EIS tests and may be plotted as a function of the State of Charge (SOC) of the cell. These electrochemical measurements help understand the dynamics of lithium plating that may occur in the cell, especially at large C-rate.

3 Theoretical Modeling

Theoretical and simulations-based analysis is carried out for an improved understanding and interpretation of experimental data, particularly towards understanding the impact of immersion cooling on cell aging. For the immersion cooling method, radiative heat dissipation is likely to be negligible due to the continuous flow of a dense liquid, such as the one used here, around the cells. This analysis first focuses on showing that radiation effects are negligible and investigating the likelihood of large temperature differentials between the core and surface of the cell. For the baseline case, the module is assumed to be surrounded by stagnant air at room temperature, with heat transfer occurring due to natural convection alone. In contrast, in cases where immersion coolant due to liquid flow around the module occurs, the dominant heat transfer is assumed to be forced convection. The central cell of the module experiences the most severe thermal conditions compared to other cells on the periphery of the module. Measured surface temperatures of all seven cells indicate that the temperature difference between cells in the module is within 1 °C for the immersed cooling case, and within 3 °C for the baseline case, with the highest temperature rise in the center cell in both cases. Therefore, all the analysis carried out in this section is based on measurements of the center cell.

Finally, the analysis carried out in this paper focuses only on the charging process, due to much higher temperatures observed during relatively faster charging than during discharge.

3.1 Analytical Modeling. In this sub-section, analytical modeling for the baseline case as well as the immersion cooling case is described.

Downloaded from http://asmedigitalcollection.asme.org/electrochemical/article-pdf/doi/10.1115/1.4063914/7063724/jeecs_21_4_041001.pdf by Southwest Research Institute user on 30 November 2023

3.1.1 Surface Temperature of the Cell. A thermal resistance network-based analysis is carried out in order to estimate the surface and core temperatures of each cell, as shown in Fig. 8. Radiation is considered only for the baseline case. Energy balance equation for an individual cell may be defined as follows:

$$mC_P \frac{dT_{\text{Cell}}}{dt} = Q_{\text{Gen}} - Q_{\text{Conv}} - Q_{\text{Rad}} \tag{1}$$

where $Q_{\text{Conv}} = (T_{\text{Cell}} - T_f)/R_{\text{Conv}}$ and $Q_{\text{Rad}} = (T_{\text{Cell}} - T_f)/R_{\text{Rad}}$ are the convective and radiative heat losses. $R_{\text{Conv}} = 1/(hA)$ and $R_{\text{Rad}} = 1/(A_{\text{Cell}}\varepsilon\sigma(T_f + T_{\text{Cell}})(T_f^2 + T_{\text{Cell}}^2))$ are the convective and radiative thermal resistances. The numerical values of various parameters used here are summarized in Table 1.

On the other hand, the heat generation rate for a single cell may be calculated by [45]

$$Q_{\text{Gen}} = I(U_{\text{OC}} - V) + I\left[T_{\text{Cell}} \frac{dU_{\text{OC}}}{dT_{\text{Cell}}}\right] = I^2 R_e + I\left[T_{\text{Cell}} \frac{dU_{\text{OC}}}{dT_{\text{Cell}}}\right] \tag{2}$$

where U_{OC} is the open circuit voltage. The first term in Eq. (2) represents irreversible heat whereas the second term shows reversible entropic heat. Finally, from Eqs. (1) and (2), a detailed energy balance equation for an individual cell may be derived:

$$m_{\text{Cell}} C_{P_{\text{Cell}}} \frac{dT_{\text{Cell}}}{dt} = I^2 R_e + I\left[T_{\text{Cell}} \frac{dU_{\text{OC}}}{dT_{\text{Cell}}}\right] - \left[\frac{T_{\text{Cell}} - T_f}{R_{\text{Conv}}}\right] - \left[\frac{T_{\text{Cell}} - T_f}{R_{\text{Rad}}}\right] \tag{3}$$

In order to determine the reversible entropic heat, the gradient of open circuit voltage as a function of cell temperature is calculated from experimental plots of open circuit voltage as a function of the state of charge and then related to the state of charge with cell temperature.

3.1.2 Surface and Core Temperature of the Cell. As shown in Fig. 8, the thermal resistance network in this problem comprises a convective and a conductive resistance in series between the fluid, cell surface, and cell core temperatures, with heat generation being supplied to the cell temperature nodes. As justified in Sec. 3 and discussed with further supporting evidence in Sec. 4, radiative heat transfer is neglected. Detailed energy balance for an individual cell considering both the surface as well as core temperatures may be written as a set of two coupled differential equations that may be solved simultaneously:

$$m_{\text{Core}} C_{P_{\text{Core}}} \frac{dT_{\text{Core}}}{dt} = I^2 R_e + I\left[T_{\text{Core}} \frac{dU_{\text{OC}}}{dT_{\text{Core}}}\right] - \left[\frac{T_{\text{Core}} - T_{\text{Surf}}}{R_{\text{Cond}}}\right] \tag{4}$$

$$m_{\text{Surf}} C_{P_{\text{Surf}}} \frac{dT_{\text{Surf}}}{dt} = \left[\frac{T_{\text{Core}} - T_{\text{Surf}}}{R_{\text{Cond}}}\right] - \left[\frac{T_{\text{Surf}} - T_f}{R_{\text{Conv}}}\right] \tag{5}$$

where $C_{P_{\text{Core}}}$ [44] and $C_{P_{\text{Surf}}}$ are heat capacities of jelly roll and metal shell, respectively, and T_{Core} and T_{Surf} are cell surface and core temperatures, respectively. Finally, R_{Cond} is the conductive thermal resistance of the jelly roll, taken from the literature to be 3.3 KW^{-1} [46]. The numerical values of these parameters are listed in Table 1.

Table 1 Numerical values of various parameters used in the simulation model

Parameter	Numerical value
C_P	715 $\text{Jkg}^{-1}\,\text{K}^{-1}$ [44]
ρ	2806 kgm^{-3}
σ	$5.67 \times 10^{-8}\ \text{Wm}^{-2}\,\text{K}^{-4}$
M	0.068 kg
m_{core}	0.06 kg
m_{Surf}	0.008 kg

Equations (3)–(5) are numerically solved using Simulink software in order to determine T_{Cell}, T_{Surf}, and T_{Core} as functions of time.

3.2 Simulink Modeling. Equations (3)–(5) are ordinary differential equations (ODEs) that govern the cell temperature distribution as a function of time. These equations are converted to a block diagram in the Simulink workspace using integrator, algebraic, and functional blocks from various libraries. ODE45 solver is used for numerical integration of the ODEs. Temperature, heat estimates, and other state data are collected into the workspace for post-processing.

3.3 Numerical Modeling. A finite volume model is developed in ANSYS Fluent in order to visualize the nature of fluid flow in the experimental setup. The geometry of the experimental setup is created in ANSYS SpaceClaim. Enclosure and battery module are modeled according to the description in Sec. 2.1. Suitable fluid domains are created to simulate fluid flow around the cells inside the enclosure. Grid independence is verified, resulting in a mesh comprising around 1.5 million nodes and 9 million elements. Only the momentum equations are solved in these simulations, since the focus is to visualize the flow field to verify and support the assumptions used in analytical modeling. Values of convective heat transfer coefficients are obtained from these simulations, for use in Simulink models described in Sec. 3.2.

4 Results and Discussion

4.1 Hypotheses for Capacity Fade. Figure 9 plots the measured percentage discharge capacity fade as a function of the number of RPTs, where an RPT is carried out at the end of every week of cycling. Each RPT in Fig. 9 represents roughly one week of calendar time and 20 fast charge cycles. It can be observed that after four RPTs, the total capacity fade in the presence of immersion cooling is around 5%, compared to 4.2% for the baseline case. The more rapid deterioration of battery capacity in the case of immersion cooling may be somewhat counter-intuitive. Based on aging data on these cells at various temperatures measured in the past, Fig. 10 shows that an average rise of temperature of around 2 °C for the immersion-cooled cells is needed to explain the increased capacity fade. The model which calculates the capacity fade for LG M50T 21700 cell cycling is deduced from an experimental data set acquired from the cell characterization testing at beginning-of-life.

The following hypotheses are tested as possible explanations for this phenomenon:

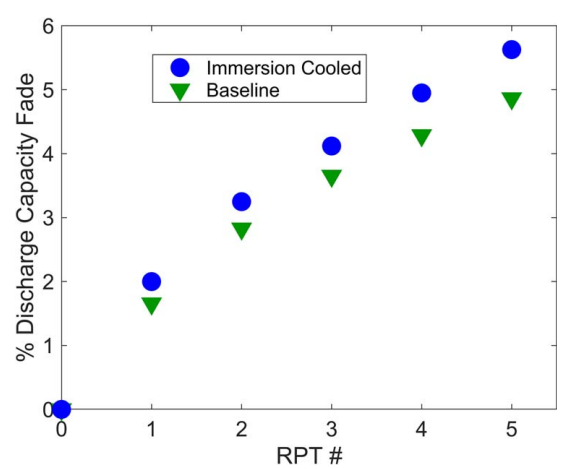

Fig. 9 Capacity fade as a function of number of RPTs. Data are shown for baseline (no cooling) as well as cooling with two different coolant fluids.

Downloaded from http://asmedigitalcollection.asme.org/electrochemical/article-pdf/doi/10.1115/1.4063914/7063724/jeecs_21_4_041001.pdf by Southwest Research Institute user on 30 November 2023

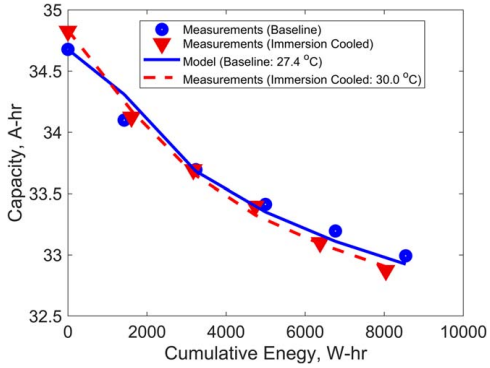

Fig. 10 Comparison of experimental data and theoretical model for capacity fade for baseline and immersion-cooled cases. Plot of capacity as a function of cumulative energy are presented. Curves based on the theoretical model for different temperatures to account for the cooling process are also shown.

(1) (Hypothesis A) Reduced radiation heat transfer due to lower emissivity caused by fluid occlusion: It has been reported [47] that certain coatings on cylindrical cells may result in high surface emissivity and thus enhanced radiation heat transfer. This may result in faster heat dissipation in the baseline case compared to the immersion cooling case.
(2) (Hypothesis B) Greater non-linear thermal gradient inside the jelly roll due to aggressive surface cooling: It has been shown [48,49] that a non-uniform thermal gradient developed inside the cell directly affects the performance and eventually deteriorates the life of the cell. The temperature gradient may result in simply a higher core temperature or an intermediate maximum inside the jelly roll if the core temperature is not significantly high. Using estimates of convective heat transfer coefficient for the baseline and immersion cooling cases in the present work, the value of the Biot number for these cases is estimated to be around 0.02 and 0.57, respectively. This indicates that there may be a temperature maxima inside the jelly roll in the immersion cooling case. Further, analytical modeling of surface-cooled and tab-cooled Li-ion battery arrangement [48,49] has shown that the tab-cooled cell has better performance despite greater operational temperature, compared to a surface-cooled cell, which has a much more non-homogeneous temperature distribution. This finding provides justification to consider this hypothesis.
(3) (Hypothesis C) It is well-known that Li-ion cells exhibit lithium plating at low temperatures [2]. The aggressive cooling in the immersion cooling case may result in the surface temperature being close to ambient even while the battery is being fast charged. This may result in increased lithium plating and higher capacity fade. EIS measurements are carried out to explore this hypothesis further.

4.2 Baseline Case Results Discussion. For baseline case experiments, the surrounding medium is stagnant air and, thus, the dominant heat transfer mechanism is natural convection around the cells, with convective heat transfer coefficient h varying as a function of air temperature [50,51]. To explore Hypothesis A discussed in Sec. 4.1, a radiative heat transfer term is considered. A suitable value for the emissivity of the outer cell surface, $\varepsilon = 0.7$ [47] is used. Surface temperature of the cell can be calculated by solving Eq. (3) in Simulink, initially considering the effect of radiative heat transfer. Referring to Fig. 11(*a*), a transient thermal distribution for the surface temperature of the cell over multiple charge–discharge cycles shows that the theoretical model that includes radiation does not match well with the experimental results. The consideration of radiative heat dissipation along with convective heat dissipation results in under-estimation of the surface temperature. On the other hand, referring to Fig. 11(*b*), without consideration of radiative heat dissipation, i.e., $\varepsilon = 0$, there is much better agreement, with a surface temperature rise of approximately 30 °C. This shows that radiation is not likely to be a dominant heat transfer mechanism in the immersion cooling conditions considered here. Based on this analysis, Hypothesis A is ruled out.

4.3 Immersion-Cooled Case Results Discussion. A comparison of experimental measurements of immersion cooling case and the analytical model based on Eq. (3) presented in Fig. 12 shows a very good agreement between the two. Due to aggressive forced convective cooling, the surface temperature of the cell rises only by 1–2 °C, compared to a 30 °C rise for the baseline case. Only convective heat transfer terms are considered in the model. From the numerical simulation model, which considered the mixed (annular and peripheral) flow effects and previous literature [50,52], a value of $h = 90\ \mathrm{Wm^{-2}\,K^{-1}}$ is extracted for the lumped convective heat transfer coefficient for use in the Simulink model above.

For a set of parameter values consistent with experimental conditions, visualization of the flow field from the Fluent model is shown in Fig. 13. The flow field is as anticipated, and low flow resistance regions are clearly delineated. There is no significant flow between the cells, indicating that the center cell has the least direct exposure to fluid. This also shows that the location of the ports can cause significant stagnant regions, leading to asymmetric cell cooling in larger battery packs. It can be observed that the flow field is a combination of annular as well as circumferential flow, i.e., an axial flow along the cell length and a radial flow around the cell radius,

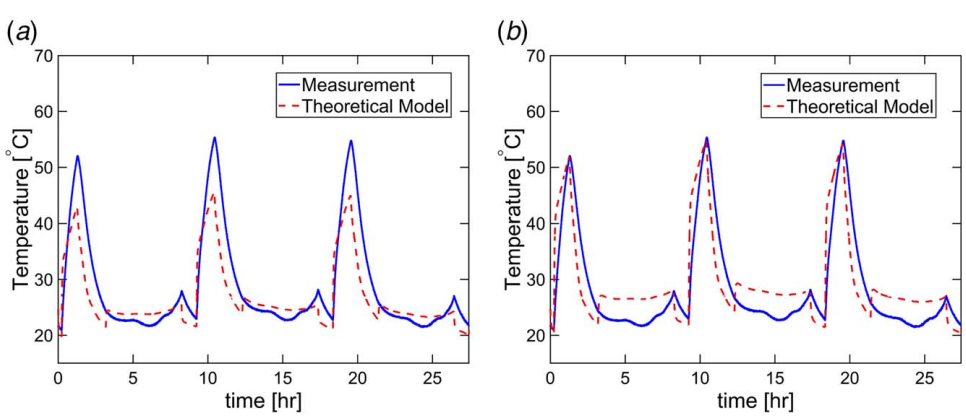

Fig. 11 (*a*) Temperature versus time for baseline case (surface temperature model) considering (*a*) convective as well as radiative heat dissipation and (*b*) only convective heat dissipation

Downloaded from http://asmedigitalcollection.asme.org/electrochemical/article-pdf/doi/10.1115/1.4063914/7063724/jeecs_21_4_041001.pdf by Southwest Research Institute user on 30 November 2023

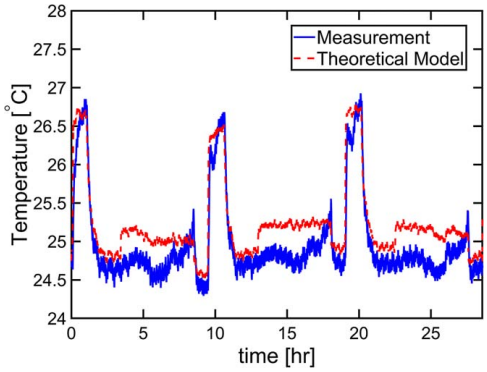

Fig. 12 Temperature versus time for immersion cooling case (Surface temperature model) considering only convective heat dissipation

respectively. The 0.5 mm gap between cells offers a much greater flow resistance compared to the 5-mm gap between cells and enclosure walls, which, in turn, promotes annular flow even if the inlet and outlet are designed to achieve circumferential flow. These results support the assumption related to the convective heat transfer coefficient to be around 90 W/m^2 K.

4.4 Cell Core Temperature Measurement Discussion. Internal temperature measurements are carried out in one of the cells in the immersed module to understand whether the core temperatures become too high during aggressive surface cooling. The goal of this experiment and analysis is mainly to explore Hypothesis B presented in the previous section. Equations (4) and (5) are solved simultaneously using Simulink to calculate the surface and core temperature of the cell, respectively. A comparison of measured and theoretically predicted internal and surface temperature is shown in Figs. 14 and 15 for baseline and immersion coolant cases, respectively. In both cases, there is good agreement for surface and core temperatures in the fast-charging region. The value of thermal conductive resistance—R_{Cond}—is based on previously reported experimental studies [46], which matched core temperature measurements with an analytical model to extract this parameter. The temperature difference between the core and surface temperatures of the cell in both cases is found to be around 1 °C, which eliminates the possibility of a higher temperature difference from the core to the surface in case of immersion cooling. As a direct result of this observation, Hypothesis B may be ruled out. It is important to note, however, that this does not fully preclude the possibility of higher temperatures in the middle of the jelly roll with low temperatures at the core and surface.

To further understand other possible unobservable internal states, a sensitivity analysis is carried out to understand the sensitivity of the temperature gradient to varying properties such as thermal

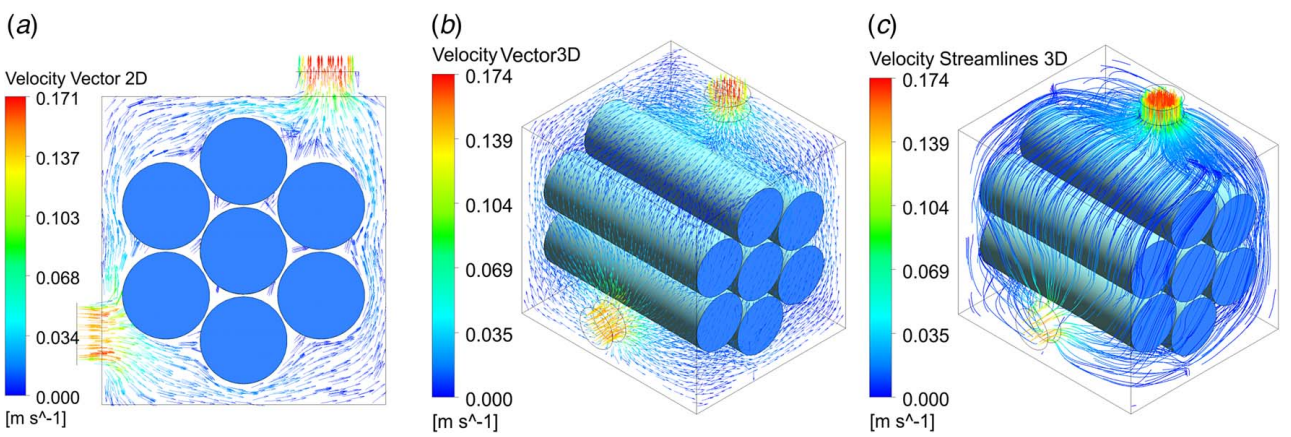

Fig. 13 Finite-element simulation results for a set of parameter values consistent with experimental conditions: (*a*) 2D velocity vectors (top view), (*b*) 3D velocity vectors, and (*c*) velocity streamlines

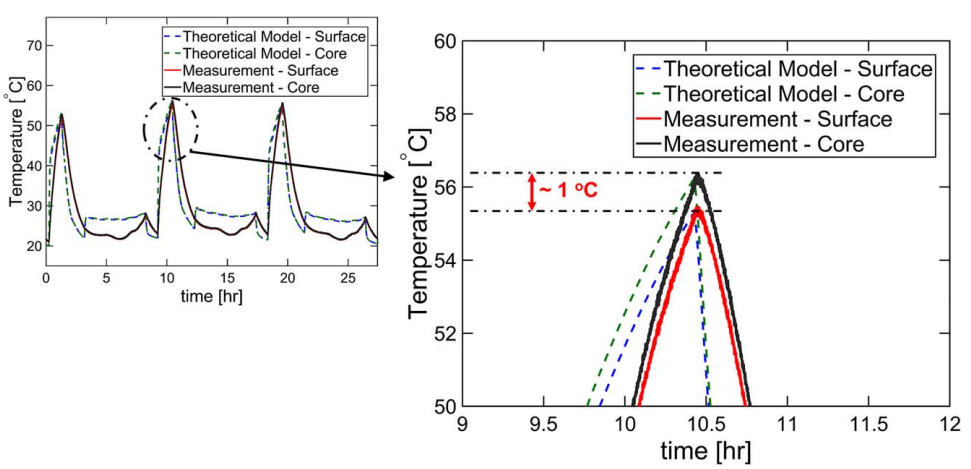

Fig. 14 Temperature versus time for baseline case (core and surface temperature model)—focusing on the difference between core and surface temperatures and comparison with experimental core and surface temperature

Downloaded from http://asmedigitalcollection.asme.org/electrochemical/article-pdf/doi/10.1115/1.4063914/7063724/jeecs_21_4_041001.pdf by Southwest Research Institute user on 30 November 2023

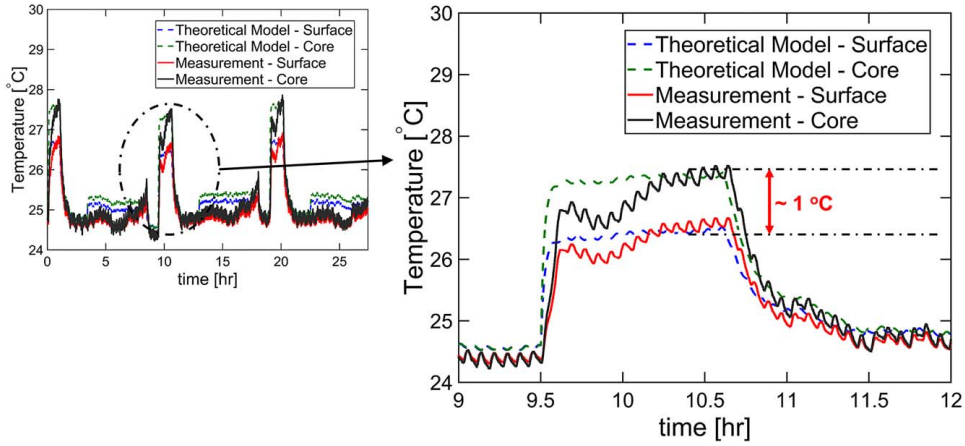

Fig. 15 Temperature vs time for immersion cooling case (core and surface temperature model)—focusing on the difference between core and surface temperatures and comparison with experimental core and surface temperature

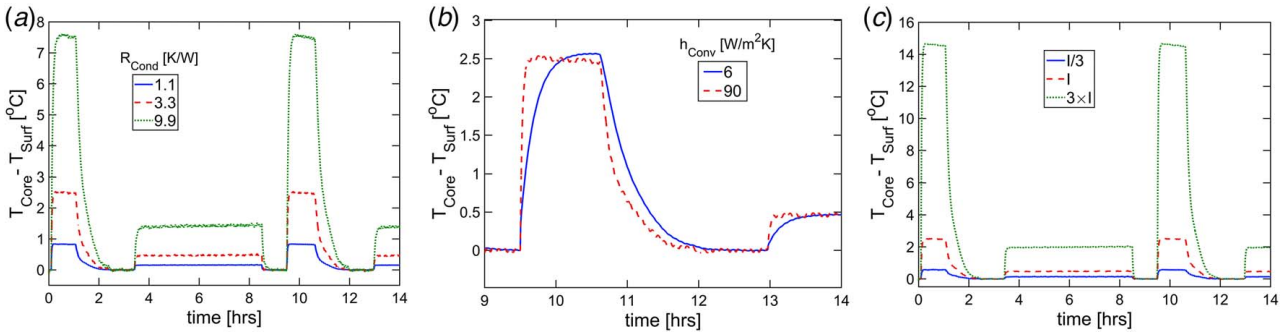

Fig. 16 Sensitivity analysis for temperature difference between core and surface to (*a*) varying conductive resistance, (*b*) varying convective heat transfer coefficient, and (*c*) varying source current

conductivity, convection heat transfer coefficient, and charge current. Results are presented in Fig. 16. It can be observed that while the core-surface temperature difference is influenced by the conduction resistance, it is largely insensitive to the value of the convective heat transfer coefficient. However, smaller values of convective heat transfer slow down the rate of temperature change, thus increasing the average temperature of the jelly roll. Charging current also has a prominent effect on the core-surface temperature difference, since heat generation in the cell directly depends on current. When interpreted in the context of fast charge rates for immersed battery packs, this result indicates that without proper thermal management, increasing charge current is detrimental to battery life due to higher internal temperatures. A key takeaway from the sensitivity analysis is related to the distribution of internal thermal conductivity of the jelly roll. The jelly roll can be considered as layers of cells in series and, as such, the thermal conductivity of each layer can change with internal temperature distribution and resistance inhomogeneity. If the thermal conductivity is thus lower in the middle of the jelly roll compared to the outer layers, this may lead to an excessive internal temperature peak. In this context, the Tesla-Panasonic 4680 cell design with dedicated tabs for inner layers may address the need to dissipate this inner heat more effectively. Unfortunately, a direct measurement is difficult since sensors are not usually embedded inside the jelly roll during manufacturing.

4.5 Electrochemical Impedance Spectroscopy Results and Lithium Plating Discussion. EIS results and analysis of beginning-of-life and aged baseline/immersion-cooled modules are shown in Fig. 17. These plots clearly show a shift in a mean resistance level, indicating aging and growth of Solid Electrolyte

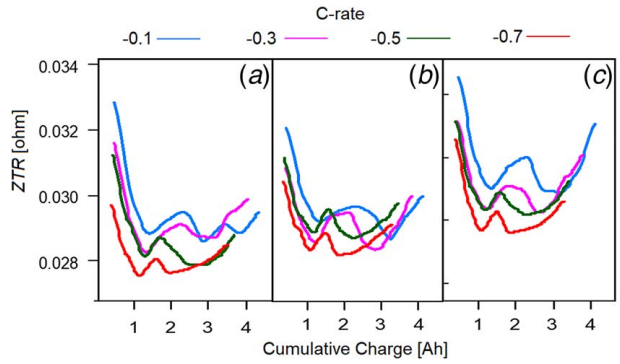

Fig. 17 ZTR as a function of cumulative charge from Pseudo-EIS measurements for (*a*) fresh cell, (*b*) cell aged in the air for 60 cycles, and (*c*) cell aged with immersion cooling for 60 cycles

Interphase (SEI), which is a thin passivation layer formed due to electrolytic reduction on the anode. These observations, along with the expected increase in temperature gradient within the cell due to immersion cooling, support Hypothesis C as the explanation behind the increased capacity fade in immersion-cooled cells. Such an influence of temperature gradient within the cell on capacity fade has been observed in past papers as well, including one that directly investigated immersion cooling [41], and another, in which an inter-electrode temperature gradient is applied through other means [53].

Moreover, the valley and peak in the middle of the *ZTR* plots for the immersion cooling case are shifted slightly to the left compared to

Downloaded from http://asmedigitalcollection.asme.org/electrochemical/article-pdf/doi/10.1115/1.4063914/7063724/jeecs_21_4_041001.pdf by Southwest Research Institute user on 30 November 2023

baseline and fresh cells. Such a shift suggests alterations in charge transfer kinetics and ion transport processes, which could be attributed to other phenomena, such as temperature-dependent changes in ion mobility and electrode kinetics under immersion cooling conditions. This subtle shift suggests that while lithium plating remains a primary contributor to the observed aging enhancement, other mechanisms might play a secondary role in the degradation process as well. Given the relatively minor nature of such a shift, it is likely that contributions from these factors toward capacity fade are minor compared to the contribution of Li plating.

EIS results and analysis of beginning-of-life and aged baseline/immersion-cooled modules presented in Fig. 17 shed light on the underlying mechanisms of battery degradation. These plots distinctly reveal a noticeable shift in the mean resistance level, which clearly indicates SEI growth and aging. In order to further investigate the fundamental reasons behind battery degradation under immersion cooling, it is essential to consider the unique thermal and electrochemical conditions of this environment. Immersion cooling exposes the cell to a consistently low operating temperature, which can promote lithium plating—a phenomenon where excess lithium ions plate onto the anode's surface during charging. This plating, if not carefully managed, can lead to the formation of dendrites and SEI thickening, contributing to increased internal resistance and reduced capacity retention over time.

In summary, while lithium plating is expected to be the primary cause for increased aging under immersion cooling observed in this work, the additional subtle shifts in EIS data point towards the intricate interplay of various electrochemical and thermal factors that influence battery performance in this unique environment. Further investigations into these mechanisms are essential for optimizing battery design and prolonging operational lifetime in such cooling scenarios.

Note that all immersion cooling measurements in this work are carried out while the cell-to-cell gap is fixed at around 0.5 mm. This small gap is representative of the goal of maximizing energy storage density. While heat removal rate from the cell may potentially increase by increasing the cell-to-cell gap due to greater coolant flow in between, this must be weighed against the resulting reduction in energy storage density.

5 Conclusions

Despite the promising nature of immersion cooling for Li-ion battery packs, several open questions remain, especially about the impact of immersion cooling on the aging of cells. The present work contributes towards addressing one of these through experimental and theoretical investigation of capacity fade caused by immersion cooling. Through a hypothesis-driven comparison of experimental measurements and theoretical modeling, a comprehensive understanding of this interesting and important phenomenon is developed. All the expected hypotheses in this study, targeting accelerated aging of cells, are examined one by one. Experimental measurements for both surface and core temperatures agree well with the respective theoretical models, for both baseline and immersion cases. EIS results indicate that lithium plating is likely to be the root cause for the observed accelerated aging in the immersion-cooled case. It is expected that the analysis in this work may contribute towards further development and eventual implementation of immersion cooling for Li-ion battery packs in a manner that provides effective thermal management with minimal potential deterioration of electrochemical performance and lifetime.

Acknowledgment

This material is partly based upon work supported by CAREER Award No. CBET-1554183 from the National Science Foundation. The authors would like to acknowledge the efforts of Mickey Argo, Barrett Mangold, and Yanyu Wang toward various aspects of testing. The testing described in this work was funded by the SwRI EVESE consortium.

Conflict of Interest

There are no conflicts of interest.

Data Availability Statement

The data sets generated and supporting the findings of this article are obtainable from the corresponding author upon reasonable request.

Nomenclature

f = frequency (Hz)
h = convective heat transfer coefficient ($\mathrm{Wm^{-2}\,K^{-1}}$)
m = mass of cell (kg)
t = time (s)
A = surface area ($\mathrm{m^2}$)
C = specific heat ($\mathrm{Jkg^{-1}\,K^{-1}}$)
I = current (A)
L = length (m)
Q = heat transfer (W)
R = thermal resistance ($\mathrm{KW^{-1}}$)
T = temperature (K)
U = open circuit voltage (V)
V = voltage (V)
R_e = electrical resistance (Ω)
ZTR = impendence at transition frequency (Ω)
ε = emissivity
σ = Stefan–Boltzmann constant, ($\sigma = 5.67 \times 10^{-8}\ \mathrm{Wm^{-2}\,K^{-4}}$)

Subscripts

Cell = cell
Cond = conduction
Conv = convection
Core = core of the cell
f = surrounding fluid
Gen = generation
OC = open circuit
P = constant pressure
Rad = radiation
Surf = surface
tr = transition

Abbreviations

BMS = battery management system
CC = constant current
CCCV = constant current constant voltage
EIS = electrostatic impedance spectroscopy
EV = electric vehicle
LPM = liters per minute
NMC = nickel manganese cobalt oxide
ODE = ordinary differential equation
PCM = phase change materials
RPT = reference performance test
SEI = solid electrolyte interface
SOC = state of charge

References

[1] Shim, J., 2002, "Electrochemical Analysis for Cycle Performance and Capacity Fading of a Lithium-Ion Battery Cycled at Elevated Temperature," J. Power Sources, **112**(1), pp. 222–230.

[2] Carter, R., and Love, C. T., 2018, "Modulation of Lithium Plating in Li-Ion Batteries With External Thermal Gradient," ACS Appl. Mater. Interfaces, **10**(31), pp. 26328–26334.

Downloaded from http://asmedigitalcollection.asme.org/electrochemical/article-pdf/doi/10.1115/1.4063914/7063724/jeecs_21_4_041001.pdf by Southwest Research Institute user on 30 November 2023

[3] Mishra, D., and Jain, A., 2021, "Multi-Mode Heat Transfer Simulations of the Onset and Propagation of Thermal Runaway in a Pack of Cylindrical Li-Ion Cells," J. Electrochem. Soc., **168**(2), p. 020504.
[4] Xia, G., Cao, L., and Bi, G., 2017, "A Review on Battery Thermal Management in Electric Vehicle Application," J. Power Sources, **367**, pp. 90–105.
[5] Shah, K., Drake, S. J., Wetz, D. A., Ostanek, J. K., Miller, S. P., Heinzel, J. M., and Jain, A., 2014, "Modeling of Steady-State Convective Cooling of Cylindrical Li-Ion Cells," J. Power Sources, **258**, pp. 374–381.
[6] Shah, K., Drake, S. J., Wetz, D. A., Ostanek, J. K., Miller, S. P., Heinzel, J. M., and Jain, A., 2014, "An Experimentally Validated Transient Thermal Model for Cylindrical Li-Ion Cells," J. Power Sources, **271**, pp. 262–268.
[7] Chalise, D., Shah, K., Prasher, R., and Jain, A., 2018, "Conjugate Heat Transfer Analysis of Thermal Management of a Li-Ion Battery Pack," J. Electrochem. Energy Convers. Storage, **15**(1), pp. 1–8.
[8] Dan, D., Yao, C., Zhang, Y., Zhang, H., Zeng, Z., and Xu, X., 2019, "Dynamic Thermal Behavior of Micro Heat Pipe Array-Air Cooling Battery Thermal Management System Based on Thermal Network Model," Appl. Therm. Eng., **162**, p. 114183.
[9] Zhang, H., Li, C., Zhang, R., Lin, Y., and Fang, H., 2020, "Thermal Analysis of a 6s4p Lithium-Ion Battery Pack Cooled by Cold Plates Based on a Multi-Domain Modeling Framework," Appl. Therm. Eng., **173**, p. 115216.
[10] Behi, H., Karimi, D., Behi, M., Ghanbarpour, M., Jaguemont, J., Sokkeh, M. A., Gandoman, F. H., Berecibar, M., and van Mierlo, J., 2020, "A New Concept of Thermal Management System in Li-Ion Battery Using Air Cooling and Heat Pipe for Electric Vehicles," Appl. Therm. Eng., **174**, p. 115280.
[11] Anthony, D., Wong, D., Wetz, D., and Jain, A., 2017, "Non-Invasive Measurement of Internal Temperature of a Cylindrical Li-Ion Cell During High-Rate Discharge," Int. J. Heat Mass. Transf., **111**, pp. 223–231.
[12] Anthony, D., Wong, D., Wetz, D., and Jain, A., 2017, "Improved Thermal Performance of a Li-Ion Cell Through Heat Pipe Insertion," J. Electrochem Soc., **164**(6), pp. A961–A967.
[13] Shah, K., and Jain, A., 2015, "Modeling of Steady-State and Transient Thermal Performance of a Li-Ion Cell With an Axial Fluidic Channel for Cooling," Int. J. Energy Res., **39**(4), pp. 573–584.
[14] Shah, K., McKee, C., Chalise, D., and Jain, A., 2016, "Experimental and Numerical Investigation of Core Cooling of Li-Ion Cells Using Heat Pipes," Energy, **113**, pp. 852–860.
[15] Lin, X., Perez, H. E., Mohan, S., Siegel, J. B., Stefanopoulou, A. G., Ding, Y., and Castanier, M. P., 2014, "A Lumped-Parameter Electro-Thermal Model for Cylindrical Batteries," J. Power Sources, **257**, pp. 1–11.
[16] Damay, N., Forgez, C., Bichat, M.-P., and Friedrich, G., 2015, "Thermal Modeling of Large Prismatic $LiFePO_4$/Graphite Battery. Coupled Thermal and Heat Generation Models for Characterization and Simulation," J. Power Sources, **283**, pp. 37–45.
[17] LeBel, F.-A., Wilke, S., Schweitzer, B., Roux, M.-A., Al-Hallaj, S., and Trovao, J. P. F., 2016, "A Lithium-Ion Battery Electro-Thermal Model of Parallelized Cells," Proceedings of the 2016 IEEE 84th Vehicular Technology Conference (VTC-Fall), Montreal, QC, Canada, Sept. 18–21, IEEE, pp. 1–6.
[18] Liu, F., Lan, F., and Chen, J., 2016, "Dynamic Thermal Characteristics of Heat Pipe via Segmented Thermal Resistance Model for Electric Vehicle Battery Cooling," J. Power Sources, **321**, pp. 57–70.
[19] Ramotar, L., Rohrauer, G. L., Filion, R., and MacDonald, K., 2017, "Experimental Verification of a Thermal Equivalent Circuit Dynamic Model on an Extended Range Electric Vehicle Battery Pack," J. Power Sources, **343**, pp. 383–394.
[20] Jiang, Z. Y., Qu, Z. G., Zhang, J. F., and Rao, Z. H., 2020, "Rapid Prediction Method for Thermal Runaway Propagation in Battery Pack Based on Lumped Thermal Resistance Network and Electric Circuit Analogy," Appl. Energy, **268**, p. 115007.
[21] Cui, X., Zeng, J., Zhang, H., Yang, J., Qiao, J., Li, J., and Li, W., 2020, "Optimization of the Lumped Parameter Thermal Model for Hard-Cased Li-Ion Batteries," J. Energy Storage, **32**, p. 101758.
[22] Ganesan, V. V., and Jain, A., 2021, "Computationally-Efficient Thermal Simulations of Large Li-Ion Battery Packs Using Submodeling Technique," Int. J. Heat Mass. Transf., **165**, p. 120616.
[23] Mohammadian, S. K., and Zhang, Y., 2015, "Thermal Management Optimization of an Air-Cooled Li-Ion Battery Module Using Pin-Fin Heat Sinks for Hybrid Electric Vehicles," J. Power Sources, **273**, pp. 431–439.
[24] Lu, Z., Meng, X. Z., Wei, L. C., Hu, W. Y., Zhang, L. Y., and Jin, L. W., 2016, "Thermal Management of Densely-Packed EV Battery With Forced Air Cooling Strategies," Energy Procedia, **88**, pp. 682–688.
[25] Akbarzadeh, M., Jaguemont, J., Kalogiannis, T., Karimi, D., He, J., Jin, L., Xie, P., van Mierlo, J., and Berecibar, M., 2021, "A Novel Liquid Cooling Plate Concept for Thermal Management of Lithium-Ion Batteries in Electric Vehicles," Energy Convers. Manag., **231**, p. 113862.
[26] Chung, Y., and Kim, M. S., 2019, "Thermal Analysis and Pack Level Design of Battery Thermal Management System With Liquid Cooling for Electric Vehicles," Energy Convers. Manag., **196**, pp. 105–116.
[27] Smith, J., Singh, R., Hinterberger, M., and Mochizuki, M., 2018, "Battery Thermal Management System for Electric Vehicle Using Heat Pipes," Int. J. Therm. Sci., **134**, pp. 517–529.
[28] Mostafavi, A., and Jain, A., 2021, "Dual-Purpose Thermal Management of Li-Ion Cells Using Solid-State Thermoelectric Elements," Int. J. Energy Res., **45**(3), pp. 4303–4313.
[29] Alaoui, C., 2013, "Solid-State Thermal Management for Lithium-Ion EV Batteries," IEEE Trans. Veh. Technol., **62**(1), pp. 98–107.
[30] Lu, M., Zhang, X., Ji, J., Xu, X., and Zhang, Y., 2020, "Research Progress on Power Battery Cooling Technology for Electric Vehicles," J. Energy Storage, **27**, p. 101155.
[31] Javani, N., Dincer, I., Naterer, G. F., and Yilbas, B. S., 2014, "Heat Transfer and Thermal Management With PCMs in a Li-Ion Battery Cell for Electric Vehicles," Int. J. Heat Mass. Transf., **72**, pp. 690–703.
[32] Yuan, X., Tang, A., Shan, C., Liu, Z., and Li, J., 2020, "Experimental Investigation on Thermal Performance of a Battery Liquid Cooling Structure Coupled with Heat Pipe," J. Energy Storage, **32**, p. 101984.
[33] Bernagozzi, M., Georgoulas, A., Miché, N., Rouaud, C., and Marengo, M., 2021, "Novel Battery Thermal Management System for Electric Vehicles With a Loop Heat Pipe and Graphite Sheet Inserts," Appl. Therm. Eng., **194**, p. 117061.
[34] He, W., Zhang, G., Zhang, X., Ji, J., Li, G., and Zhao, X., 2015, "Recent Development and Application of Thermoelectric Generator and Cooler," Appl. Energy, **143**, pp. 1–25.
[35] Wu, S., Lao, L., Wu, L., Liu, L., Lin, C., and Zhang, Q., 2022, "Effect Analysis on Integration Efficiency and Safety Performance of a Battery Thermal Management System Based on Direct Contact Liquid Cooling," Appl. Therm. Eng., **201**, p. 117788.
[36] Patil, M. S., Seo, J.-H., and Lee, M.-Y., 2021, "A Novel Dielectric Fluid Immersion Cooling Technology for Li-Ion Battery Thermal Management," Energy Convers. Manag., **229**, p. 113715.
[37] Wang, Y., Rao, Z., Liu, S., Li, X., Li, H., and Xiong, R., 2021, "Evaluating the Performance of Liquid Immersing Preheating System for Lithium-Ion Battery Pack," Appl. Therm. Eng., **190**, p. 116811.
[38] Tan, X., Lyu, P., Fan, Y., Rao, J., and Ouyang, K., 2021, "Numerical Investigation of the Direct Liquid Cooling of a Fast-Charging Lithium-Ion Battery Pack in Hydrofluoroether," Appl. Therm. Eng., **196**, p. 117279.
[39] "Product Specification: Rechargeable Lithium Ion Battery (Model : INR21700 M50 18.20Wh)", https://www.dnkpower.com/wp-content/uploads/2019/02/LG-INR21700-M50-Datasheet.pdf. Accessed September 17, 2023.
[40] Drake, S. J., Martin, M., Wetz, D. A., Ostanek, J. K., Miller, S. P., Heinzel, J. M., and Jain, A., 2015, "Heat Generation Rate Measurement in a Li-Ion Cell at Large C-Rates Through Temperature and Heat Flux Measurements," J. Power Sources, **285**, pp. 266–273.
[41] Lechner, B., Benezeder, F., Golubkov, A., Rasch, B., Scheiber, A., Winder, L., Zitz, C., Potenza, R., and Prentice, G., 2023, "Immersion vs Indirect Cooling: A Comparison of Battery Thermal Management Approaches: Fast-Charging, Battery Lifetime, and Thermal Propagation Performance," Proceedings of the 44th International Vienna Motor Symposium, Wien, Austria, Apr. 26–28, https://graz.elsevierpure.com/en/publications/immersion-vs-indirect-cooling-a-comparison-of-battery-thermal-man
[42] Gaberšček, M., 2021, "Understanding Li-Based Battery Materials via Electrochemical Impedance Spectroscopy," Nat. Commun., **12**(1), p. 6513.
[43] Koleti, U. R., Dinh, T. Q., and Marco, J., 2020, "A New On-Line Method for Lithium Plating Detection in Lithium-Ion Batteries," J. Power Sources, **451**, p. 227798.
[44] Parhizi, M., Ahmed, M. B., and Jain, A., 2017, "Determination of the Core Temperature of a Li-Ion Cell During Thermal Runaway," J. Power Sources, **370**, pp. 27–35.
[45] Hales, A., Marzook, M. W., Bravo Diaz, L., Patel, Y., and Offer, G., 2020, "The Surface Cell Cooling Coefficient: A Standard to Define Heat Rejection From Lithium Ion Battery Pouch Cells," J. Electrochem Soc., **167**(2), p. 020524.
[46] Forgez, C., Vinh Do, D., Friedrich, G., Morcrette, M., and Delacourt, C., 2010, "Thermal Modeling of a Cylindrical $LiFePO_4$/Graphite Lithium-Ion Battery," J. Power Sources, **195**(9), pp. 2961–2968.
[47] Hatchard, T. D., MacNeil, D. D., Stevens, D. A., Christensen, L., and Dahn, J. R., 2000, "Importance of Heat Transfer by Radiation in Li-Ion Batteries During Thermal Abuse," Electrochem. Solid-State Lett., **3**(7), p. 305.
[48] Troxler, Y., Wu, B., Marinescu, M., Yufit, V., Patel, Y., Marquis, A. J., Brandon, N. P., and Offer, G. J., 2014, "The Effect of Thermal Gradients on the Performance of Lithium-Ion Batteries," J. Power Sources, **247**, pp. 1018–1025.
[49] Zhao, Y., Patel, Y., Zhang, T., and Offer, G. J., 2018, "Modeling the Effects of Thermal Gradients Induced by Tab and Surface Cooling on Lithium Ion Cell Performance," J. Electrochem. Soc., **165**(13), pp. A3169–A3178.
[50] Incropera, F. P., DeWitt, D. P., Bergman, T. L., and Lavine, A. S., 1996, *Fundamentals of Heat and Mass Transfer*. Wiley, New York.
[51] Churchill, S. W., and Chu, H. H. S., 1975, "Correlating Equations for Laminar and Turbulent Free Convection From a Horizontal Cylinder," Int. J. Heat Mass. Transf., **18**(9), pp. 1049–1053.
[52] Churchill, S. W., and Bernstein, M., 1977, "A Correlating Equation for Forced Convection From Gases and Liquids to a Circular Cylinder in Crossflow," J. Heat Transfer, **99**(2), pp. 300–306.
[53] Carter, R., Kingston, T. A., Atkinson, R. W., Parmananda, M., Dubarry, M., Fear, C., Mukherjee, P. P., and Love, C. T., 2021, "Directionality of Thermal Gradients in Lithium-Ion Batteries Dictates Diverging Degradation Modes," Cell Rep. Phys. Sci., **2**(3), p. 100351.

Downloaded from http://asmedigitalcollection.asme.org/electrochemical/article-pdf/doi/10.1115/1.4063914/7063724/jeecs_21_4_041001.pdf by Southwest Research Institute user on 30 November 2023